AGU PUBLICATIONS

JGR

Journal of Geophysical Research: Atmospheres

RESEARCH ARTICLE

10.1002/2013JD020266

Key Points:
- Investigation into the structure of X-ray emissions was completed
- Maximum X-ray source region radii were between 2 and 3 m
- Leaders displayed consistency with both compact and diffuse electron sources

Correspondence to:
M. M. Schaal,
meagan.schaal@gmail.com

Citation:
Schaal, M. M., et al. (2014), The structure of X-ray emissions from triggered lightning leaders measured by a pinhole-type X-ray camera, *J. Geophys. Res. Atmos.*, *119*, 982–1002, doi:10.1002/2013JD020266.

Received 22 MAY 2013
Accepted 25 DEC 2013
Accepted article online 4 JAN 2014
Published online 30 JAN 2014

The structure of X-ray emissions from triggered lightning leaders measured by a pinhole-type X-ray camera

M. M. Schaal[1], J. R. Dwyer[1], S. Arabshahi[1], E. S. Cramer[1], R. J. Lucia[1], N. Y. Liu[1], H. K. Rassoul[1], D. M. Smith[2], J. W. Matten[2], A. G. Reid[2], J. D. Hill[3], D. M. Jordan[4], and M. A. Uman[4]

[1]Department of Physics and Space Sciences, Florida Institute of Technology, Melbourne, Florida, USA, [2]Physics Department and Santa Cruz Institute for Particle Physics, University of California, Santa Cruz, California, USA, [3]Team QNA, ESC-25, Kennedy Space Center, Orlando, Florida, USA, [4]Department of Electrical and Computer Engineering, University of Florida, Gainesville, Florida, USA

Abstract We investigate the structure of X-ray emissions from downward triggered lightning leaders using a pinhole-type X-ray camera (XCAM) located at the International Center for Lightning Research and Testing. This study builds on the work of Dwyer et al. (2011), which reported results from XCAM data from the 2010 summer lightning season. Additional details regarding the 2010 data are reported here. During the 2011 summer lightning season, the XCAM recorded 12 out of 17 leaders, 5 of which show downward leader propagation. Of those five leaders, one dart-stepped leader and two chaotic dart leaders are the focus of this paper. These three leaders displayed unique X-ray emission patterns: a chaotic dart leader displayed a diffuse structure (i.e., a wide lateral "spraying" distribution of X-rays), and a dart-stepped leader and a chaotic dart leader exhibited compact emission (i.e., a narrow lateral distribution of strong X-ray emission). These two distinct X-ray emission patterns (compact and diffuse) illustrate the variability of lightning leaders. Using Monte Carlo simulations, we show that the diffuse X-ray source must originate from a diffuse source of energetic electrons or possibly emission from several sources. The compact X-ray sources originate from compact electron sources, and the X-ray source region radius and electric charge contained within the X-ray source region were between 2 and 3 m and on the order of 10–4 C, respectively. For the leaders under investigation, the X-ray source region average currents were determined to be on the order of 102 A.

1. Introduction

Despite a decade of research, much remains unknown about the nature of the source region of lightning leaders that produce X-ray emissions. Based upon time of arrival position and time measurements [*Howard et al.*, 2008, 2010] of X-ray pulses associated with leader steps, it has been inferred that X-rays may originate from the streamer zones (a volume filled by filamentary corona streamers) in front of the leaders. However, the size of the X-ray source region has never been quantitatively measured. Because the X-rays are produced by energetic electrons, knowing the size of the source region for the former provides information about the distribution of the latter. The runaway electron distribution, in turn, follows the field lines of the high electric field region, helping to determine the lightning charge distribution. While some earlier papers discussed details regarding the length of the streamer zone [*Gorin et al.*, 1976; *Bazelyan et al.*, 1978; *Idone*, 1992; *Petrov and D'Alessandro*, 2002; *Biagi et al.*, 2009; *Hill et al.*, 2012], the actual width or radius is still unknown. *Idone* [1992], using UV streak photography, observed the streamer zone, or what they called a "diffuse, hemispherical corona brush," extending 5–10 m above an upward positive leader during an altitude triggered lightning strike. *Bazelyan et al.* [1978] determined the streamer zone to be 100–200 m in front of a negative stepped leader tip. *Petrov and D'Alessandro* [2002] determined that the streamer zone must reach a length of at least 0.7 m before a leader initiation could be observed. *Bazelyan et al.* [2009] determined streamer zone lengths to be between 3 and 16 m for nine leaders in a Florida triggered lightning discharge, and that the streamers extended to the sides and along the front of the leader channel. *Hill et al.* [2012], used high-speed video imagery to observe downward negative leaders with streamer zone lengths of about 25 m. They also found that the lengths of the streamers zones were longer for chaotic dart leaders than for dart or dart-stepped leaders. Dart and dart-stepped leaders exhibited visible fan-shaped emission regions and features such as space stems and space leaders [*Biagi et al.*, 2010; *Hill et al.*, 2011]. The observation of longer streamer zone lengths associated with chaotic dart leaders was used to suggest that HF electromagnetic field pulses were being emitted from multiple, vertically displaced locations along the leader

channel nearly simultaneously. Furthermore, *Hill* [2012] showed that X-rays are located on the order of 10 m below the causative dE/dt sources (using flat plate antennas). It should be noted that dart, dart-stepped, and chaotic dart leaders exhibit differences in their X-ray and dE/dt waveforms. Typically, dart leaders emit a short burst of relatively weak energetic radiation prior to the start of the return stroke with relatively slow electric field changes (hundreds of microseconds). Dart-stepped leaders emit discrete bursts of energetic radiation at intervals of 1–2 μs with colocated dE/dt pulses. Chaotic dart leaders not only display the same electric field variations as dart leaders but also show series of tens of nanosecond length dE/dt pulses. Additionally, chaotic dart leaders appear to display a continuous burst of energetic radiation usually during the 10 μs prior to the onset of the return stroke [*Hill et al.*, 2012].

Dwyer et al. [2011] published the first high-speed X-ray images of triggered lightning leaders. These images provided new information about how energetic electrons are accelerated by lightning, potentially identifying some details about the high-field regions and the sources of X-rays and gamma rays (X-rays in the MeV range, not to imply originating from nuclear decays). Four flashes were recorded by the X-ray camera (XCAM) in 2010, but not all of the leaders generated enough X-rays to produce statistically significant images (i.e., images that have enough X-ray photons so that the statistical fluctuations are low). However, one chaotic dart leader showed a downward propagating leader when viewed in X-rays. The tip of the lightning leader channel produced the greatest amount of X-ray emission, with an additional diffuse glow surrounding the channel. The diffuse glow was common in all X-ray images from 2010. It was suggested that the diffuse glow could be caused by X-ray emission from a diffuse source (such as streamer zones) or from Compton scattering of X-rays emitted from the leader front. Hard X-rays penetrating the XCAM's 1.27 cm thick lead shield, which encased the entire instrument, could also cause this diffuse glow, because the lead shielding becomes transparent for X-rays with energies above about 400 keV.

Although some questions regarding the source of the X-ray emission have been clarified, the analysis presented by *Dwyer et al.* [2011] was only qualitative and did not quantify the size and structure of the emission region. In this paper, we report new details about the structures of the X-ray source regions provided by X-ray camera images from the 2010 and 2011 lightning seasons. In addition, using these images and Monte Carlo simulations of energetic electron and X-ray propagation, we estimate the magnitude of the electric charge within the X-ray source region. During the 2011 summer lightning season, the XCAM recorded 12 out of 17 leaders, 5 of which show downward leader propagation and produced images that had enough X-ray photons so that the statistical fluctuations were low. Of those five, one dart-stepped leader and two chaotic dart leaders are the focus of this paper. These three leaders, which displayed unique X-ray emission patterns (i.e., a narrow and a wide lateral spraying distribution of X-rays as seen in the XCAM), are described in this report. Using Monte Carlo simulations of the propagation of X-rays through air, it will be shown that a chaotic dart leader appears to have a diffuse electron source with X-ray emissions not consistent with a point source of energetic electrons. Additionally, we present the maximum X-ray source region radius, the maximum electric charge contained within the X-ray source region, and the current contained within the source region for one dart-stepped and one chaotic dart leader.

2. Instrumentation

The XCAM measures energetic radiation in the form of X-rays and gamma rays (energies ranging from 30 keV to several megaelectron volts) from rocket-triggered lightning and has been in operation since 2010. The XCAM is located at the International Center for Lightning Research and Testing (ICLRT) at the Camp Blanding Army National Guard Base in North Central Florida and is operated jointly by the University of Florida and Florida Institute of Technology. Further details about the ICLRT and other instrumentation located on the site are described in *Howard et al.* [2008], *Saleh et al.* [2009], *Howard et al.* [2010], *Hill et al.* [2012], *Hill* [2012], and *Schaal et al.* [2012].

The XCAM images X-rays from lightning by using a lead mask with a restricted "pinhole" aperture. The X-ray emission that is detected by the camera, located on the ground, originates from a vertical lightning channel created from rocket-triggered lightning. The channel is only vertical (or near vertical) beneath the wire top, which is typically 200–400 m in altitude. The camera is shielded by 1.27 cm thick lead on all sides except for the front, which is shielded by 2.54 cm of lead. A 7.62 cm diameter "pinhole" is located at the front of the camera (Figure 1). Lead sheets are mounted to a welded 0.64 cm thick steel box to absorb the lead's

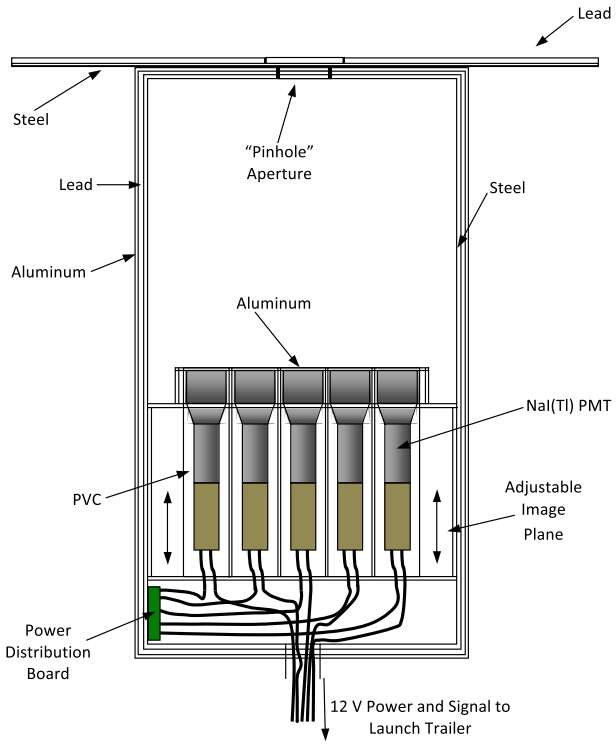

Figure 1. Schematic diagram (not to scale) of a "pinhole" type X-ray camera located at the ICLRT. The camera is 0.64 m wide and 1.25 m long with 1.27 cm thick lead sheets completely surrounding the camera on all sides except for a 7.62 cm diameter pinhole at the front of the camera. Lead sheets are mounted to a welded 0.64 cm thick steel box to absorb the lead's fluorescent emission lines. This structure is then wrapped in 0.32 cm thick aluminum to keep out RF noise, water, and light. Inside the XCAM, the image plane is adjustable giving a field of view anywhere from about ±20° to ±40° in both the horizontal and vertical directions. The elevation can be adjusted between 0° and 50° and aimed anywhere that is desired. The image plane consists of 30 NaI/photomultiplier tube (PMT) scintillators. Each NaI/PMT detector contains a 7.62 cm × 7.62 cm cylindrical scintillator that is optically coupled to the photomultiplier tube (adapted from *Dwyer et al.* [2011]).

fluorescent emission lines. This structure is then wrapped in 0.32 cm thick aluminum to keep out RF noise, water, and light.

Inside the instrument, the image plane is adjustable giving a field of view (FOV) ranging from about ±20° to ±40° in both the horizontal and vertical directions. The elevation can be adjusted between 0° and 50°. The image plane consists of 30 NaI/PMT (photomultiplier tube) detectors. Each detector contains a 7.62 cm × 7.62 cm cylindrical NaI scintillator that is optically coupled to the PMT. Both the pinhole and the detectors have the same diameter to prevent overlap in the FOV. Each NaI/PMT combination is also connected to a PMT base that produces a signal via the anode. These detectors display a fast light decay time constant of about 250 ns at room temperature from the NaI scintillator.

When the XCAM is armed, the detectors are powered by a 12 V battery. The 30 anode signals are transmitted via 20 m long, 50 Ω double-shielded BNC cables from the camera to two, 16-channel, Yokogawa DL 750 Scopecorders within the electronics box mounted next to the camera. Two seconds of data with 1 s of pretrigger sampling are recorded at a sampling rate of 10 million samples per second for both scopes. The amplitudes of the NaI/PMT signals are limited to ±5 V due to the limitation by the Yokogawa oscilloscopes. The oscilloscopes recording the XCAM instrument outputs are triggered by an electrical current measurement, which is split between the two scopes to provide accurate time alignment.

3. Modeling

Natural and triggered lightning produce runaway electrons and bremsstrahlung X-rays in strong electric fields as the electrons interact with air molecules [*Dwyer et al.*, 2005]. To model these phenomena, detailed Monte Carlo simulations of runaway electron propagation of air were used and the characteristics of the energetic electron source populations were investigated. Generally, energetic electrons are injected into the simulations and propagated until their energy falls below the detection threshold of the instrument

(30 keV). As the energetic electrons propagate through air, they undergo both inelastic and elastic scattering. They also emit bremsstrahlung X-ray photons. The models propagate the photons until they are absorbed or dropped below an energy of 30 keV, which is approximately the minimum energy that can pass through the 0.32 cm thick aluminum cover and reach the NaI detectors. When the photons enter the camera box, their detection angles and energies are determined. The simulations, which have a spherical geometry when the electrons are injected into the model, are compared to the 2-D observations from the X-ray camera.

Additionally, the simulations account for all interactions affecting energetic electrons and positrons, which involve energy losses through ionization and atomic excitation, Mτller scattering for secondary electron production, and Bhabha scattering [*Dwyer et al.*, 2003; *Dwyer*, 2004, 2007; *Dwyer and Smith*, 2005]. Photon interactions including photoelectric absorption, Rayleigh and Compton scattering, and pair production are also modeled. In addition, bremsstrahlung production of X-rays and gamma rays from all secondary electrons and positrons and gamma rays from positron annihilation are also simulated.

The simulation has been broken up into two stages: (1) propagation in the air and (2) entry into the instrument because the instrument is far from the source and too many of the simulation's products (photons) would fail to come in contact with the instrument if it was run in one stage. Two different simulations were also used for modeling in the paper: REAM (runaway electron avalanche model, adapted from the Monte Carlo models from *Dwyer et al.* [2003], *Dwyer* [2004, 2007], and *Dwyer and Smith* [2005]) and GEANT3, a simulation software based on the Monte Carlo method. Stage one of REAM and stage two of GEANT3 were used to produce the modeled results shown in Figures 11, 12, and 19, whereas both stages one and two of GEANT3 were used to produce the modeled results shown in Figures 4, 10, 14, 15, 17, and 18. GEANT3 is always used for the second stage because it is easy to code a complex instrument (including interactions with lead, steel, aluminum, and the NaI scintillators), whereas both REAM and GEANT3 are used for the first stage. GEANT3's first stage of simulations uses a point source of electrons (no electric field), which are emitted isotropically. REAM is used for the first stage specifically because an electric field can be introduced and a source radius, r_0, can be allowed to vary between simulations. For the first stage of the REAM model, the electric field is assumed to be radial (field vectors pointing radially inward) in a spherical coordinate system and to fall off as $1/r^2$. The electrons (500,000 of them) are emitted radially from a spherical charge region of radius, r_0 at the leader tip. The Earth's magnetic field has been demonstrated to have no significant effect on the simulation's results [*Dwyer and Smith*, 2005].

Since X-rays are associated with stepping in natural lightning, the source is expected to be located near the strong electric fields at the leader tip. Thus, in the first stage of the REAM model, energetic electrons are assumed to be located in this high-field region (a radial electric field for this case) and allowed to propagate outward away from the leader tip. In the first stage of both models, the spectrum of the energetic electrons was assumed to be initially of the form $dN_e/dK \propto \exp(-K/K_0)$, where K is the kinetic energy of the runaway electrons [*Lehtinen et al.*, 1999; *Dwyer*, 2004]. This assumption was motivated by the exponential energy spectrum with an *e*-folding kinetic energy, K_0, of 7.3 MeV produced during relativistic runaway electron avalanche (RREA) multiplication. In this study, K_0 was allowed to vary and was chosen to best fit the XCAM data.

Further details of the model including the determination of the maximum radius of the source region will be described later in this paper.

4. XCAM Observations and Results

In this report, following the approach of *Dwyer et al.* [2011], 2-D observations (in the *xz* plane) are presented in terms of emission and observation time. If not otherwise noted, labels in the following figures designated as "time" are considered to be the observation time. Emission time is the time that the X-rays are emitted from the source, whereas observation time is the time that X-rays are measured by the NaI/PMTs inside the camera. The emission time is calculated by subtracting the time that it takes for the X-rays to propagate from the lightning channel to the NaI detectors (calculated from the speed of light). The time measured at the launcher when the return stroke peak current rises to half of its peak value is defined as $t = 0$.

The 30 NaI/PMT anode signals are converted to colored images by assigning each detector to a pixel (shown as a hexagon) of the camera as shown in Figure 2. Figure 2 shows a 15 μs waveform that was

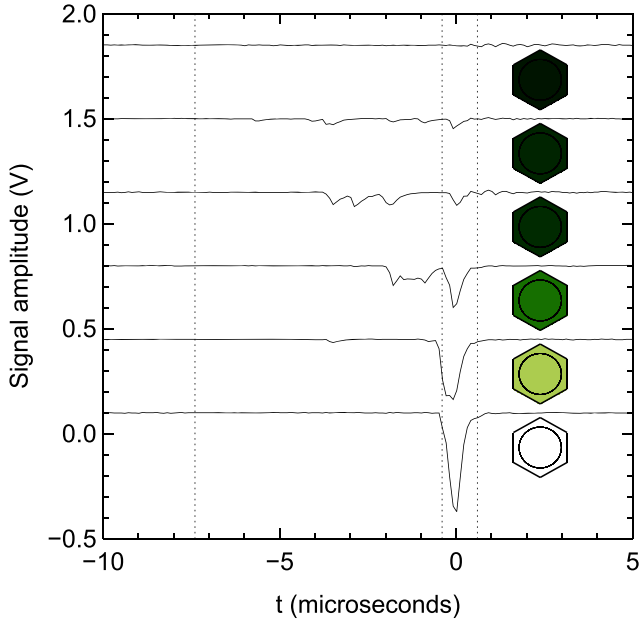

Figure 2. A 15 μs waveform that displays how anode signals are converted to colored images by assigning each detector to a pixel (shown as a hexagon) of the camera for the triggered chaotic dart leader from UF 10-21. Six NaI/PMTs are shown at varying viewing angles corresponding to roughly 12 m (bottom) to 300 m (top) above the ground. The circles within the colored hexagons represent the size of the NaI detector faces. The circular shape of the NaI scintillators have been changed to hexagons in the images. Each negative pulse corresponds to a single X-ray photon or multiple detections of X-ray photons, which were converted to colors in the images. The larger the amplitude of the pulse indicates a lighter-colored pixel. A pulse height of 0.05 V corresponds to 662 keV of energy (adapted from *Dwyer et al.* [2011]).

recorded from a triggered chaotic dart leader. Six measurements from NaI/PMTs are shown at varying viewing angles corresponding to roughly 12 m (bottom) to 300 m (top) above the ground. The circles within the colored hexagons represent the size of the NaI/PMT detector faces. For clarity, the circular shape of the NaI scintillators have been changed to hexagons in the images [*Dwyer et al.*, 2011]. Each negative pulse corresponds to a single X-ray photon (or multiple detections of X-ray photons), which was then converted to colors in the images. A larger pulse amplitude is indicated by a lighter-colored pixel. A pulse height of 0.05 V corresponds to 662 keV of energy, which was determined by a Cs-137 radioactive calibration source. For identification and location purposes, the NaI/PMTs have been numbered and are visualized in Figure 3. These NaI/PMT numbers will be referred to as such in later sections.

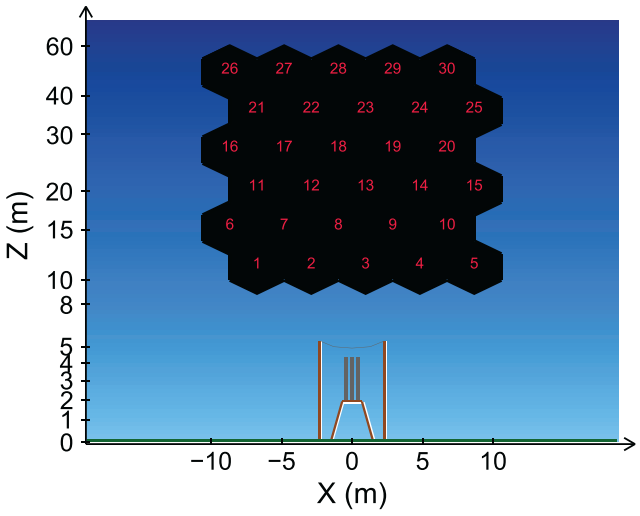

Figure 3. NaI/PMTs detectors numbered for identification and location purposes. The elevation angle is about 44°.

During the 2011 lightning season, the X-ray camera was positioned 23 m away from the rocket launcher. The image plane was adjusted to allow a FOV of about ±22° (vertical and horizontal) and an elevation angle of about 44°. The XCAM triggered on five lightning flashes (12 leaders), but only five leaders had sufficient X-ray intensities for imaging. For this study, we chose to analyze three leaders in detail, UF 11-35 L2 (L is short for leader number), a chaotic dart leader; UF 11-35 L5, another chaotic dart leader; and UF 11-34 L1, a dart-stepped leader. UF refers to a rocket-triggered flash and is followed by the year, e.g., 11, and flash number, e.g., 35. The letter L, plus a number, refers to the specific leader/return

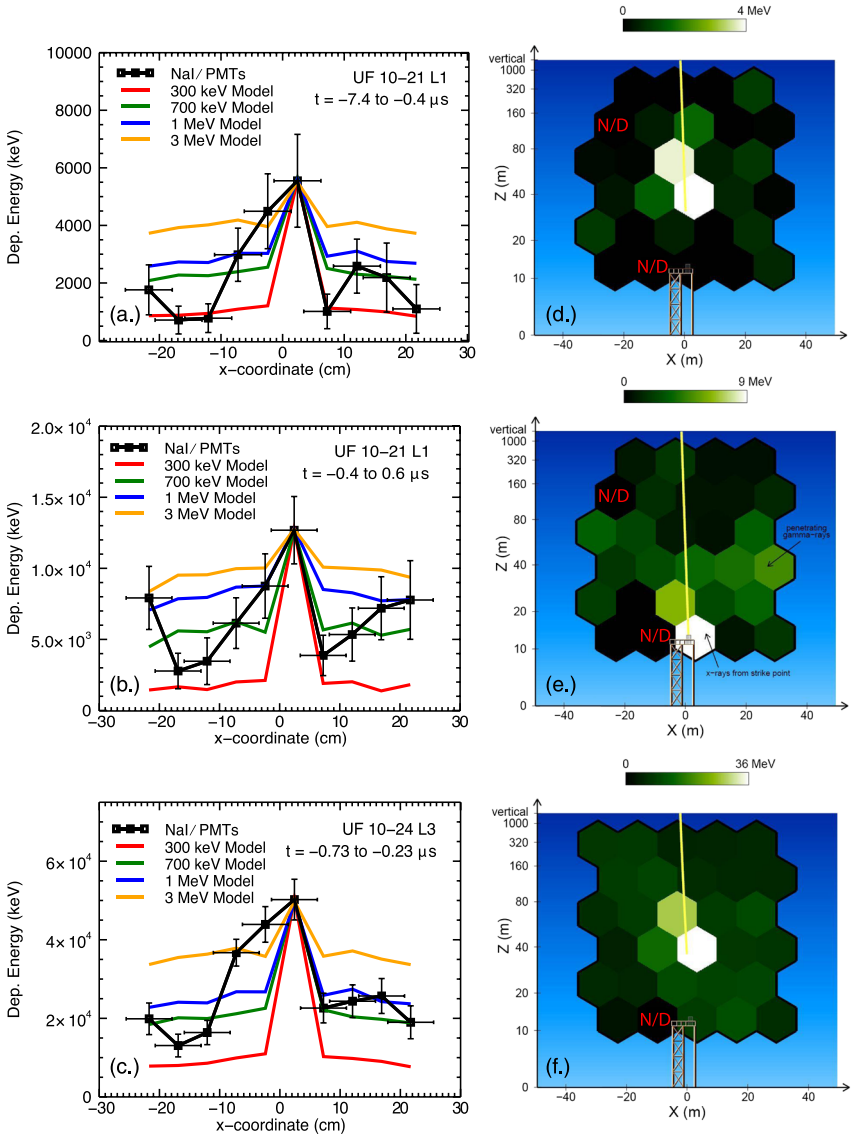

Figure 4. (a–f) The total deposited energy from the two triggered chaotic dart leaders. Figures 4d–4f show the images directly from *Dwyer et al.* [2011]. Figures 4a–4c show the lateral deposited energy distribution (*x* coordinate) of X-rays that were measured from the 30 NaI/PMTs. Each value in Figures 4a–4c is an average over the number of functioning NaI/PMT detectors in a column. Modeled lateral deposited energy distributions at different *e*-folding energies (300 keV, 700 keV, 1 MeV, and 3 MeV) are fit to the measured energies on these plots. For these simulations, the point source of electrons and the X-ray emission is assumed to be centered at tube 13 shown in Figures 4a, 4c, 4d, and 4f; and tube 3 shown in Figures 4b and 4e. Figures 4a and 4d show the deposited X-ray energy (UF 10-21 L1) from −7.4 μs to −0.4 μs prior to the start of the return stroke. Figures 4b and 4e show observation times from −0.4 μs to 0.6 μs. Figures 4c and 4f show the deposited energies from the leader UF 10-24 L3.

stroke sequence in that flash. Only certain time frames within the three leaders were chosen to be analyzed because they lacked saturation and contained low statistical fluctuations.

4.1. Follow-Up From *Dwyer et al.* [2011]

Four triggered flashes (three chaotic dart leaders, two dart-stepped leaders, and three dart leaders) were analyzed in *Dwyer et al.* [2011]. Monte Carlo simulations were added (see Figure 4) in this paper to address the questions that could not be answered from *Dwyer et al.* [2011]. Although *Dwyer et al.* [2011] provided new insights into lightning propagation and energetics, a substantial diffuse component was visible in the detectors surrounding the channels, which could not be explained without modeling. It was suggested that the diffuse X-ray component could be due to hard X-rays penetrating the camera's lead mask or from a diffuse source.

Table 1. The 2011 Lightning Leaders Analyzed in This Paper

Leader ID	Leader Type	Description	Associated Figures
UF 11-24 L1	Chaotic Dart	Displays saturation in tubes	5
UF 11-34 L1	Dart-Stepped	Displays a compact structure	5–12
UF 11-34 L2	Dart-Stepped	Displays a compact structure	5
UF 11-35 L2	Chaotic Dart	Displays a compact structure	5, 16–19
UF 11-35 L5	Chaotic Dart	Displays a diffuse structure	5, 13–15

Figure 4 shows the total deposited energy from two out of the three triggered chaotic dart leaders from *Dwyer et al.* [2011]. Figures 4d–4f (and their corresponding time windows) are the plots directly from *Dwyer et al.* [2011]. Figures 4a–4c show the lateral deposited energy distribution (x coordinate) of X-rays that were measured from the 30 NaI/PMTs. Each data point in Figure 4 represents the energy per detector deposited at some lateral distance. Each value is an average over the number of functioning NaI/PMT detectors in a column (e.g., the data point at $x = 2$ cm corresponds to the mean of tubes 3, 13, and 23). In other words, the total deposited energy on all of the tubes in each column was divided by the number of tubes in that column. The error bars in the energy are determined by Monte Carlo simulations that are used to predict the number of photons detected, since they are not known in the measurements. These simulations can estimate the average energy per photon, which is then used in combination with the measured deposited energies to calculate the number of photons detected. The number of photons detected is then used to determine the approximate RMS variations (error bars) that should occur in the deposited energies. Here the error bars were determined from the simulation results that use the 300 keV model. Modeled lateral deposited energy distributions are also fit to the measured energies on these plots, which include all instrumental effects (penetrating X-rays and Compton scattering of X-ray in air or in the camera from the leader front). These simulations are modeled using an exponential spectrum with electrons emitted isotropically originating from a point source at various *e*-folding energies. For these simulations, the source of the electron and X-ray emissions is assumed to be centered on tube 13 for Figures 4a and 4c and tube 3 for Figure 4b because they contain the highest X-ray intensity.

Figures 4a and 4d display the deposited X-ray energy (UF 10-21 L1) from −7.4 μs to −0.4 μs prior to the start of the return stroke. Since the simulations emit electrons from a point source, the modeled energies in the distributions around the $x = 0$ cm (in Figures 4a and 4d) show a peak in deposited energy. The deposited energies in the background NaI/PMTs (the NaI/PMTs that are located to the left and right of the leader channel) also are nonuniform. This may be due to random fluctuations of the deposited energies in the background tubes because each tube measures only a few high-energy X-rays. Figures 4b and 4e show

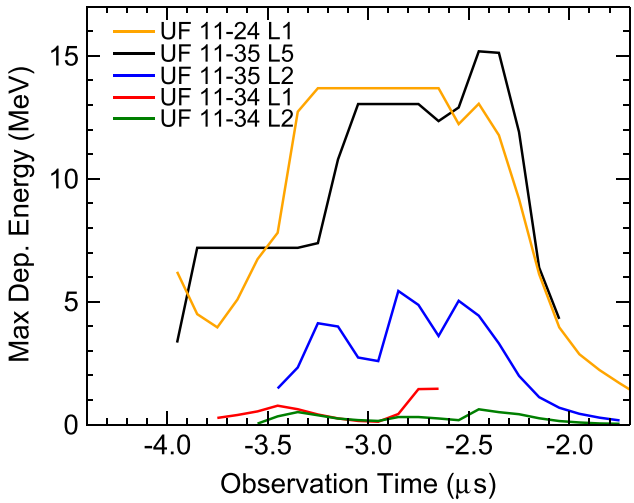

Figure 5. Five leaders that were recorded by the XCAM during the 2011 summer lightning season. UF 11-34 L1, UF 11-35 L2, and UF 11-35 L5 are the three leaders analyzed in detail. The peak deposited energy per 0.1 μs over all 30 NaI/PMTs versus the camera's observation time is shown. The maximum deposited energies (y axis) are the energies recorded while the leader channel was located in the FOV of the X-ray camera. Horizontal lines in the deposited energies represent time periods of detector saturation. Since the lightning leaders vary in speed, so do the durations of the observation times.

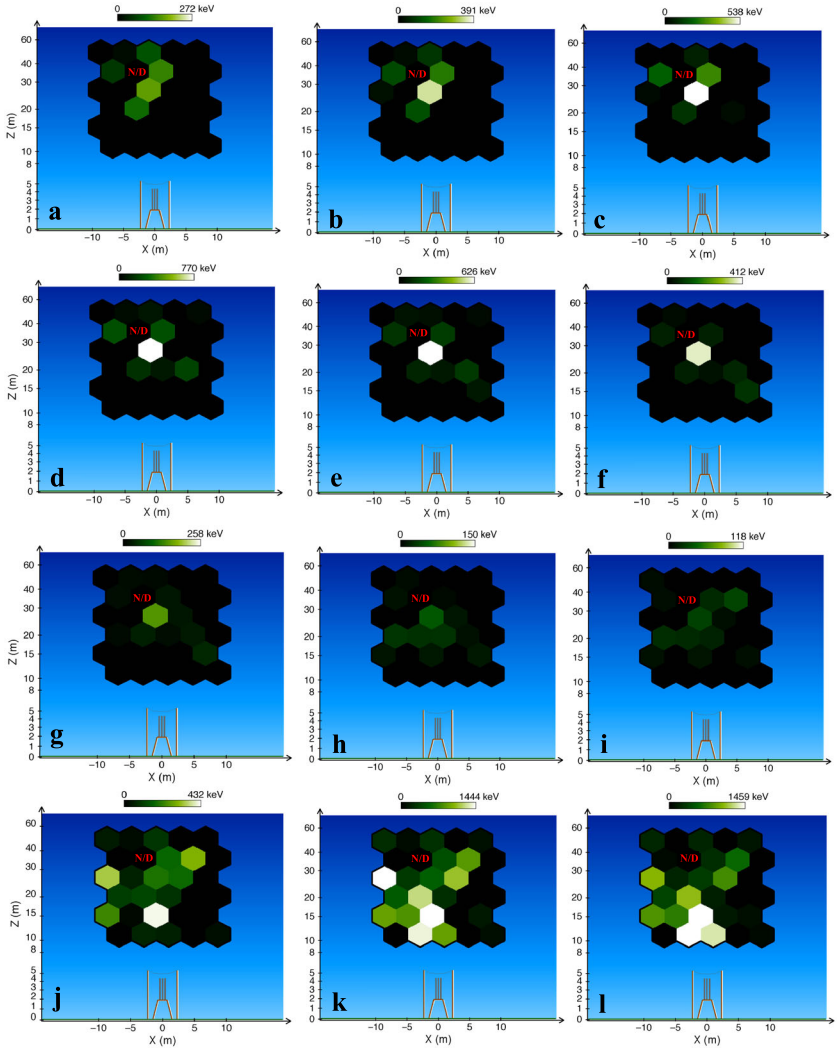

Figure 6. Successive 0.1 μs timed images of UF 11-34 L1 as it passed through the camera's FOV (from an altitude of about 60 m to about 8 m). The color scale has been adjusted so that the detector with the maximum deposited energy appears closest to white. The exposure covers the observation times of −3.8 to −2.7 μs. The rocket launcher is illustrated at the bottom. It should be noted that one of the detectors was not operational and so is labeled N/D (no data) in the images.

the same leader, but for observation times from −0.4 μs to 0.6 μs. Figure 4b also displays nonuniform background energies. Figures 4c and 4f show the deposited energies from the leader UF 10-24 L3. This leader displays a nonuniform background energy similar to UF 10-21 L1.

Based on the energy fluctuations in the background tubes, hard X-rays are most likely penetrating the XCAM's lead front as shown in Figure 4. As described in *Dwyer et al.* [2011], the diffuse component arrives simultaneously with the bright attachment component. This suggests that the diffuse component could be located no more than 10 m from the source region of the attachment. Given that the X-ray path length cannot be different by more than 10 m, it suggests that this large contribution is unlikely to be from Compton scattering of X-rays in air. Additionally, since the deposited energy in background tubes (compared to the model) do not reach an energy greater than 1 MeV, the results from Figure 4 can rule out a characteristic energy greater than 3 MeV. For Figures 4a and 4c, the total number of runaway electrons that fits the measured energies is on the order of 10^{10}-10^{11} electrons (using *e*-folding energy models between 300 keV and 1 MeV). For Figure 4b, the total number of runaway electrons that fits the measured energies is on the order of 10^{10} electrons (using *e*-folding energy models between 300 keV and 1 MeV).

4.2. 2011 Lightning Leaders

During the 2011 summer lightning seasons, five leaders were analyzed with the XCAM (see Table 1). The maximum deposited energy for all 30 NaI/PMTs versus the camera's observation time can be seen for these

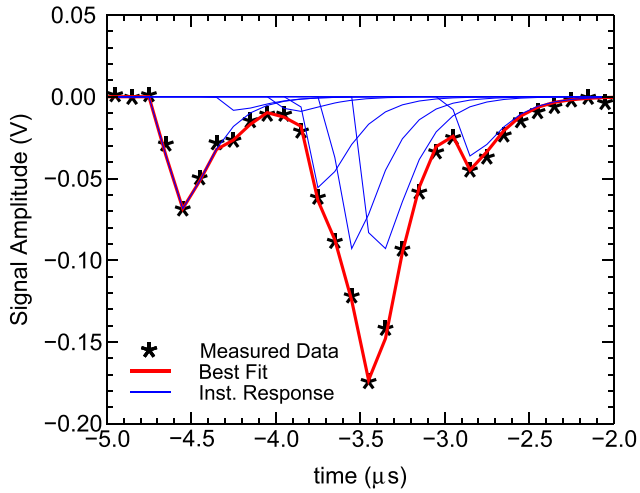

Figure 7. The raw X-ray waveform (black markers) from tube 18 from UF 11-34 L1. A signal amplitude of 0.05 V corresponds to a measured deposited energy of 662 keV. The overall best fit is shown in red. The shape of the blue curves originates from an analytical function from the electronics of the PMT base. Closer investigation of the X-ray emission from tube 18 shows that pulse pileup is occurring. Several photons are piled up within this emission. The maximum energy of each of these photons appears to be about 1 MeV. However, each of these 1 MeV photons could be composed of several low-energy photons.

five leaders in Figure 5. This figure is shown to summarize the deposited energy ranges of the 2011 leaders and to show which leaders produce saturation in some detectors. The deposited energies, in Figure 5, are the energies recorded while the leader channel was located in the FOV of the X-ray camera. Since the lightning leaders vary in speed, so do the durations of the observation times. It should be noted that for UF 11-24 L1 and UF 11-35 L5 some detectors saturate in certain time frames. The time frames with saturation were not analyzed. Additionally, UF 11-35 L2 seems to display an oscillation in the maximum deposited energy as it propagates through the FOV of the camera, but this could be due to how the tubes are arranged.

Of the five leaders, one dart-stepped leader (UF 11-34 L1) and two chaotic dart leaders (UF 11-35 L2 and UF 11-35 L5) displayed unique X-ray emission patterns. UF 11-35 L5 displayed a diffuse structure (i.e., a wide lateral spraying distribution of X-rays spanning at least 12 m or 3 detector tubes) (see Figure 13), and UF 11-34 L1 and UF 11-35 L2 showed a compact emission region (i.e., a narrow lateral distribution of strong X-ray emission spanning about 4 m or 1 detector tube) (see Figures 6 and 16).

4.2.1. UF 11-34 L1

Figure 6 shows successive 0.1 μs timed images of UF 11-34 L1 as it passed through the camera's FOV (from an altitude of about 60 m to about 8 m). This leader has been classified as a dart-stepped leader (see *Hill* [2012]) but contains a higher than normal dart-stepped leader speed (about 10^7 m s^{-1}) and exhibits dE/dt pulse fluctuations that are indicative of some type of stepping mechanism. The dE/dt pulses, which are associated with stepping, are not as clear as a typical dart-stepped leader. Additionally, the waveforms from UF 11-34 L1 are not at all similar to a typical chaotic dart leader. Thus, the higher observed leader speed of UF 11-34 L1 may be a result of it not being a "classical" dart-stepped leader but perhaps really one of those "in between" cases. The exposure covers the observation times of −3.8 to −2.7 μs. It should be noted that one of the detectors was not operational and so is labeled N/D (no data) in the images. Figure 6a–6i shows time windows during which the dart-stepped leader appears to produce X-ray emission continuously detected by the same pixel (tube 18). There are six 0.1 μs time windows with significant X-ray emission recorded in tube 18. Other pixels displayed X-ray emission at these times, but significant X-ray emission was only seen in tube 18. To explain the continuous X-ray emission, the raw X-ray waveform (black markers) from tube 18 is shown in Figure 7. A signal amplitude of 0.05 V corresponds to a measured deposited energy of 662 keV. The overall best fit is shown in red. The shape of the blue curves originates from an analytical function from the NaI light output and the electronics of the PMT base [*Knoll*, 2000]. Closer investigation of the X-ray emission from tube 18 shows that pulse pileup is occurring (due to the pulses arriving within the 0.25 μs decay time to be resolved individually). Several photons are piled up within the main pulse. The maximum energy of each of these photons appears to be about 1 MeV. However, each of these 1 MeV pulses

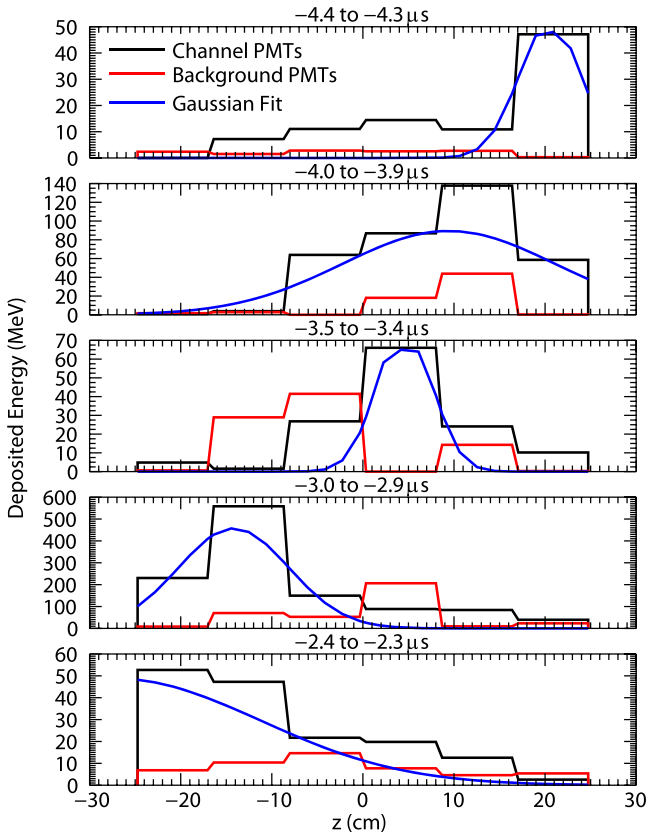

Figure 8. A histogram from select time frames (not all time frames shown here) of the X-ray emission from UF 11-34 L1, which was fit to a Gaussian distribution for each microsecond to produce the average position of the peak. The average positions are used to find the height of the source versus time. The black data show the PMTs viewing the lightning leader channel. The red data show the remaining background PMTs. As time progresses, the leader channel NaI/PMTs are shown to move from $z = 25$ cm to $z = -25$ cm in the image plane.

could be composed of several low-energy photons. The source region must be confined to a small area for such strong emission to be detected in only one of the detectors.

In order to find the speed of UF 11-34 L1 in the FOV, the deposited energies from the background NaI/PMTs (tubes: 1, 4, 5, 6, 10, 11, 14, 15, 16, 20, 21, 24, 25, 26, 27, 29, and 30) were subtracted from the average deposited energies of the tubes containing the lightning leader channel (tubes: 2, 3, 7, 8, 9, 12, 13, 17, 18, 19, 23, and 28). The histogram (see Figure 8) of the X-ray emission for each time period (in this case about 0.1 μs time windows) was then fit to a Gaussian distribution to produce the average position of the peak. The black data show the PMTs viewing the lightning leader channel. The red data shows the remaining background PMTs. As time progresses, the leader channel NaI/PMTs are shown to move from $z = 25$ cm to $z = -25$ cm in the image plane. The average positions were used to find the height of the source versus time as shown in Figure 9 [*Dwyer et al.*, 2011]. As this leader moves through the FOV, it appears to change speed. The three leader velocities observed were: (a) -7.35×10^6 m/s, (b) -2.36×10^7 m/s, and (c) -1.22×10^6 m/s. A portion of the X-ray emission from Figure 9 is most likely out of the FOV.

Figure 10 displays an image of deposited energies from UF 11-34 L1 similar to Figures 4a–4c. Figure 10 shows a 0.1 μs time window, which corresponds to Figure 6d. Five models with varying *e*-folding energies are also shown. These simulations are modeled with the center located at tube 18 and an exponential spectrum with electron emission originating from a point source. The simulations show that the measured deposited energies are consistent with a point source of energetic electron emission. A fluctuation of deposited energies is seen in the background NaI/PMTs, making it difficult to discern the *e*-folding energy. However, if the background level on the right side of the peak in Figure 10 is used, it appears that the emission has an *e*-folding energy between 300 and 700 keV. This would imply that the larger deposited energies on the left side could be due to the extended size of the source region.

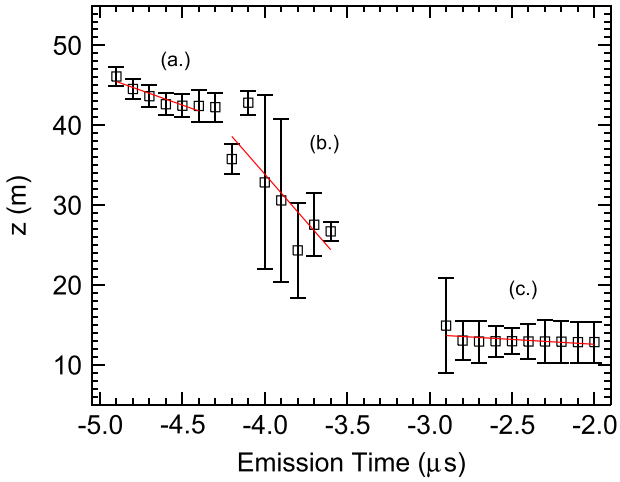

Figure 9. The leader speed found using the X-ray camera for the dart-stepped leader of UF 11-34. As the leader moves through the FOV, the leader appears to change speed. The following are a list of the three leader velocities (determined by the best-fit lines in red) seen: (a) -7.35×10^6 m/s, (b) -2.36×10^7 m/s, and (c) -1.22×10^6 m/s. Some of the X-ray emission from Figure 9a is most likely out of the FOV. It should be noted that the data points between −3.5 and −3.0 μs were removed due to large errors due to very few photons.

The maximum radius of the X-ray source region (tube 18 from Figure 6d) was also estimated. The maximum source region radius is defined here as the largest that the radius of the source region could be and still be consistent with the X-ray emission measured on all of the tubes. As stated earlier, it has been inferred that X-rays may be emitted from the streamer zone in front of the leader, and so the X-ray source region is most likely the streamer zone. Figure 11 shows how the maximum radius of the source region was calculated. Since the brightest X-ray emission (from Figure 6d) appears to originate from location of tube 18, Monte Carlo simulations with varying *e*-folding energies and source radii were modeled using tube 18's altitude as the origin. Even though it has been shown [*Hill*, 2012]that X-rays are located on the order of 10 m below the causative d*E*/d*t* sources (which are presumably the major step current locations), tube 18 extends about 20 m in the *z* direction, which likely means that multiple, vertically displaced X-ray pulses are included in a single tube. In Figure 11, the plane radial distance of 0 cm is the center of tube 18 in the XCAM's coordinates. Models were produced with *e*-folding energies of 150 keV, 300 keV (Figure 11), 700 keV, 1 MeV (Figure 11), 1.2 MeV, and 1.5 MeV and source radii of 0.1 m, 0.5 m, 1.0 m, 2.0 m, 5.0 m, and 10.0 m. The modeled deposited energies are displayed (in Figure 11) with the measured deposited energies of the radial falloff of energy from the center of tube 18. The 30 NaI/PMT deposited energies are binned according to their radial distances and displayed as black markers in Figure 11. The deposited energies are also

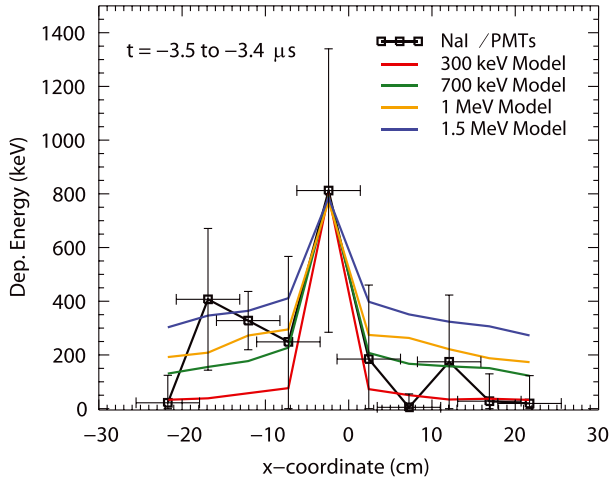

Figure 10. A 0.1 μs time window of deposited energies from UF 11-34 L1 similar to Figures 4a–4c. Five models with varying *e*-folding energies are also shown. These simulations are modeled with the center being at tube 18 and an exponential electron emission spectrum from a point source.

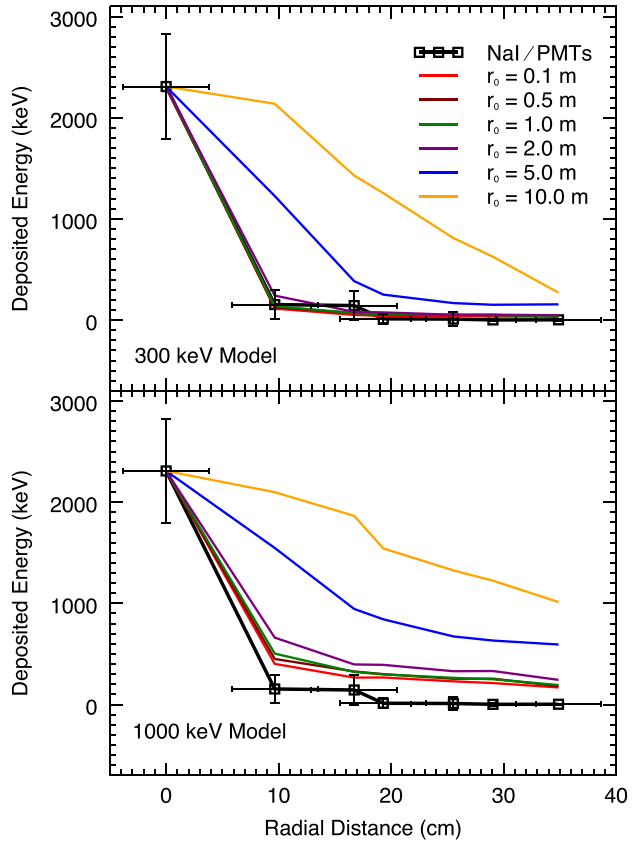

Figure 11. Radial distance, in XCAM coordinates, of the deposited energy from time window −3.5 to −3.4 μs from UF 11-34 L1. The radial distance of 0 cm is the center of tube 18 in the XCAM's coordinates. Models were produced with *e*-folding energies of 150 keV, (top) 300 keV, 700 keV, (bottom) 1 MeV, 1.2 MeV, and 1.5 MeV and source region radii of 0.1 m, 0.5 m, 1.0 m, 2.0 m, 5.0 m, and 10.0 m. The NaI/PMTs are binned and displayed as black markers. The deposited energies are also normalized since each bin might contain more than one tube. The modeled energies were fit to the first binned marker located at the radial distance of 0 cm.

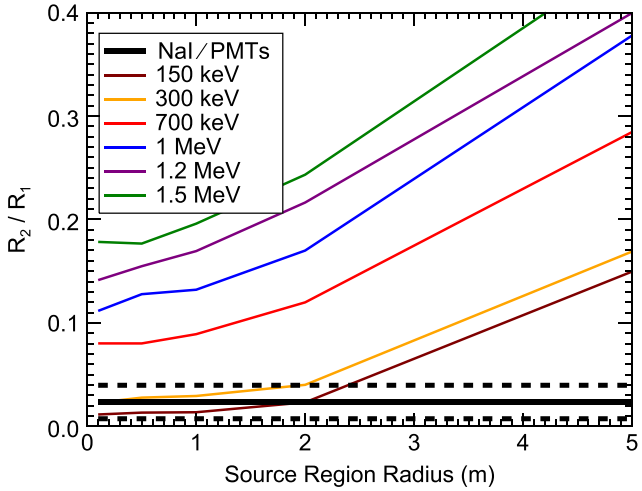

Figure 12. The ratio of R_2/R_1 versus the approximate source region radius (discrete radii, see Figure 11) for UF 11-34 L1. The ratio of energy bin numbers 2–7 (R_2 equal to the mean of the energies at 9.5 cm, 17 cm, 19 cm, 25.5 cm, 29 cm, and 35 cm in Figure 11) were divided by energy bin number 1 (R_1 equal to the deposited energy at 0 cm in Figure 11). Ratios were determined for the measured deposited energies, for all of the modeled energies in Figure 11, and at the other *e*-folding energies (not shown). The black line is the measured energy ratio for the time window from Figure 6d (−3.5 to −3.4 μs). The dashed lines indicate the error bars. The colored lines show models of varying *e*-folding energies and how R_2/R_1 (from the XCAM's coordinates) changes with varying source region radius.

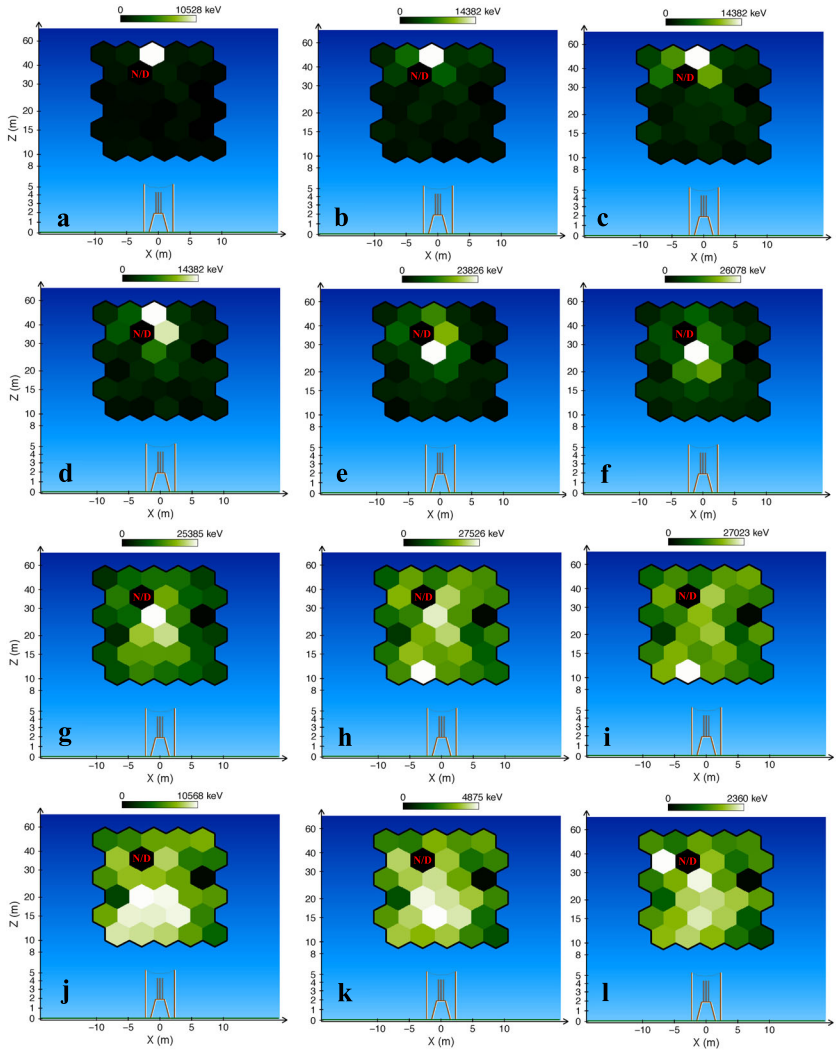

Figure 13. Successive 0.2 μs timed images of UF 11-35 L5 as it passed through the camera's FOV. The exposure covers the observation times of −4.0 to −1.8 μs. Frames g and j display a diffuse structure (i.e., wide lateral spraying distribution of X-rays as seen in the X-ray camera to span at least 12 m or three XCAM detector tubes) with its source in the FOV.

normalized by the total number of tubes in that bin because each bin might contain more than one tube. The modeled energies were fit to the first binned marker located at the radial distance of 0 cm.

To help discern the maximum radii of the source regions and the approximate *e*-folding energy, a ratio of the energies was determined. The energy in bin numbers 2–7 (labeled R_2, which is equal to the mean of the energies of the tubes at 9.5 cm, 17 cm, 19 cm, 25.5 cm, 29 cm, and 35 cm) were divided by the energy in bin number 1 (labeled R_1, which is equal to the deposited energy of the tube at 0 cm). Ratios were determined for the measured deposited energies, for all of the modeled energies in Figure 11, and at all other *e*-folding energies (not shown). The ratio, R_2/R_1, versus the approximate radius of the source region is shown in Figure 12. The black line is the measured deposited energy ratio from the 0.1 μs time windows from Figure 6d. The colored lines show models of the varying *e*-folding energies and how the R_2/R_1 (from the XCAM's coordinates) changes with varying source radii. Based on this figure, the largest possible source radius for this particular time window is about 2.4 m with an *e*-folding energy of 150 keV. For any *e*-folding energy below 150 keV the maximum source radius does not change significantly and so was not included in Figure 12. The results from Figure 12 also exclude *e*-folding energies higher than about 700 keV.

4.2.2. UF 11-35 L5

Figure 13 shows successive 0.2 μs timed images of UF 11-35 L5 as it passed through the camera's FOV. The exposure covers the observation times of −4.0 to −1.8 μs. Figures 13g and 13j display a diffuse structure (i.e., a wide lateral spraying distribution of X-rays) with their source regions in the FOV.

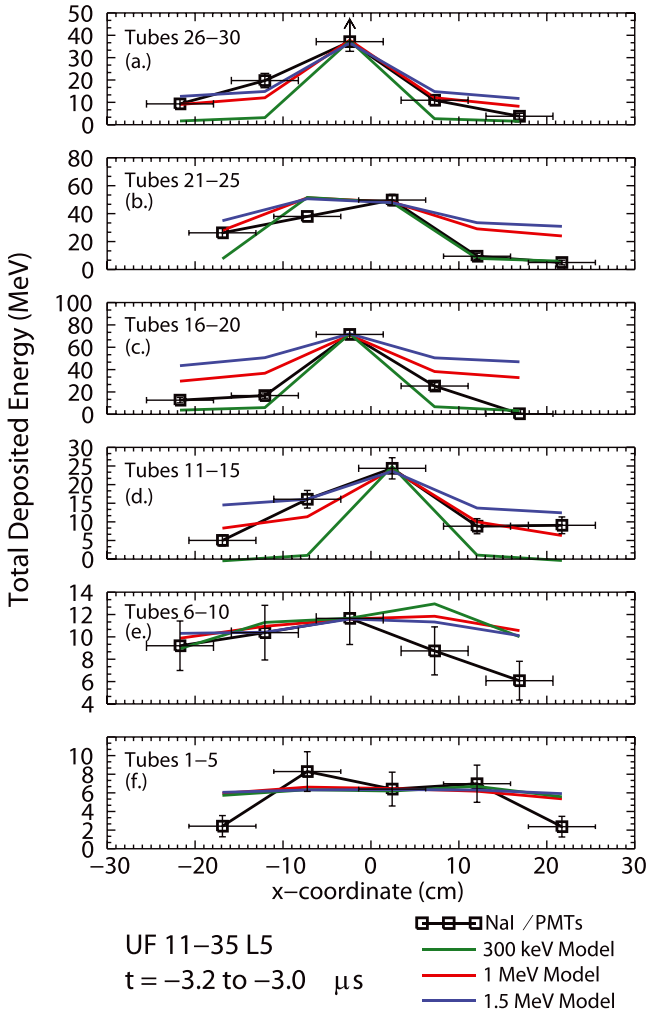

Figure 14. (a–e) The lateral deposited energy distribution of the NaI/PMTs divided into six plots corresponding to differing altitudes for the time window from −3.2 to −3.0 μs from UF 11-35 L5. Figure 14a corresponds to about 50 m (at the tube's center), while Figure 14f corresponds to about 10 m. Figure 14 shows the same time frame as Figure 13e. The models were chosen to have their sources centered at the following tubes: tube 28, between tubes 22 and 23, tube 18, and tube 13.

Figure 14 shows the lateral deposited energy distribution of the NaI/PMTs divided into six plots corresponding to differing altitudes for the time window from −3.2 to −3.0 μs. Figure 14a corresponds to about 50 m, while Figure 14f corresponds to about 8 m. Figure 13e shows the same time frame as Figure 14 but is shown pictorially. To account for the broken tube (tube 22, see Figure 13), we have averaged the surrounding data points on this figure to estimate what the deposited energy should be in this location. This has also been done in Figures 15, 17, and 18. The models were chosen to have each of their sources centered at the following tubes: tube 28, between tubes 22 and 23, tube 18, and tube 13. Keep in mind that each model (with sources at varying tube locations) originates from a point source of electron emission. The deposited energies from each tube in the four models were added together to form one combined model of deposited energy in order to find the model that best fits the measured deposited energy distribution. Combining these models together essentially makes a vertical line of sources tens of meter long and best fits the measured deposited energies. This supports *Hill et al.* [2011], which suggested that HF electromagnetic field pulses were being emitted from multiple vertically displaced locations along the leader channel. The result of this summed model appears to underestimate the width of the measured deposited energy distributions near the center at $x = 0$ cm in Figures 14a– 14f and overestimates the background deposited energies at $x = -15$ cm and 15 cm, suggesting that the source region (spatially) is diffuse. This feature is especially clear in Figures 14c and 14d. Figure 14a shows saturation in tube 28, so no determinations about the structure of the X-ray emission can be attained from this panel.

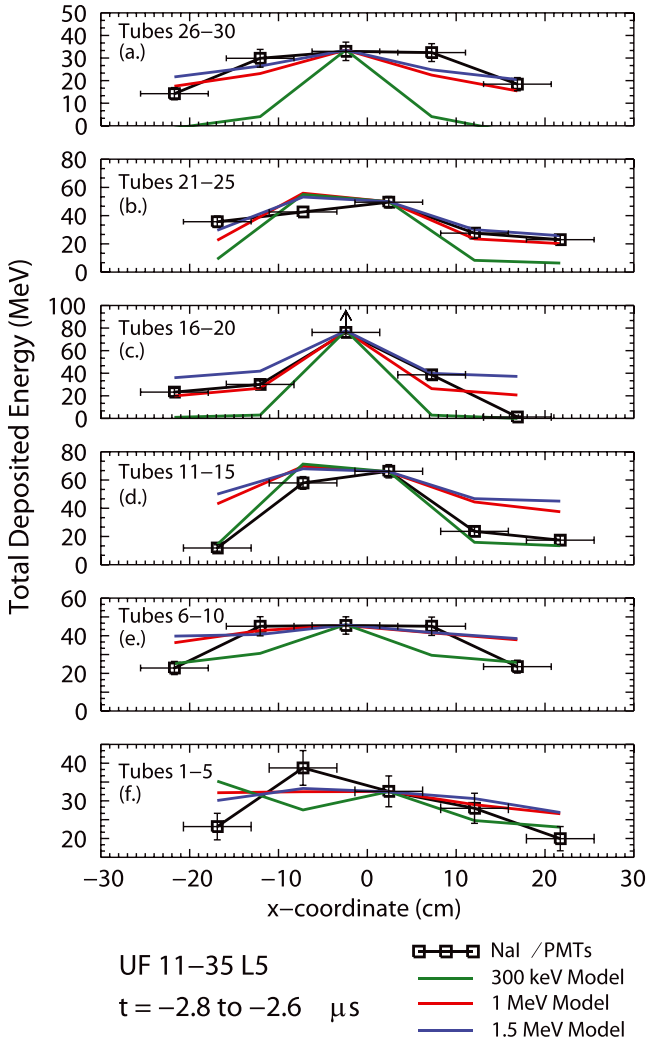

Figure 15. A −2.8 to −2.6 μs exposure (from UF 11-35 L5) of the lateral deposited energy distribution of the NaI/PMTs divided into six plots corresponding to differing altitudes similar to Figure 14. This figure corresponds to Figure 13g. The models were chosen to have their sources centered at the following tubes: tube 18, between tubes 22 and 23, and between tubes 12 and 13.

Figure 15 shows the lateral deposited energy distribution of the NaI/PMTs divided into six plots corresponding to differing altitudes similar to Figure 14. This figure corresponds to Figure 13g or a time window from −2.8 to −2.6 μs. The models were chosen to have their sources centered at the following tubes: between tubes 22 and 23, tube 18, and between tubes 12 and 13. The modeled energies also underestimate the width of the peak near $x = 0$ cm. Figure 15c shows saturation in tube 18. Specifically, the deposited energy distributions in Figures 15a and 15e do not fit at any *e*-folding energy distributions further suggesting that the source might be wider than what the models expects. This agrees with Figure 13g, which also shows an appearance of a wider energy distribution.

4.2.3. UF 11-35 L2

Figure 16 shows X-ray emission of UF 11-35 L2 for two differing durations. Figures 16a and 16b show the observation exposures from −2.9 to −2.8 μs and −3.5 to −1.8 μs. The X-ray source region moves downward through the entire FOV of the XCAM to make the pattern of illuminated tubes seen in Figure 16b.

Figures 17 and 18 show the lateral deposited energy distribution of the NaI/PMTs divided into six plots corresponding to differing altitudes for the time window from −2.9 to −2.8 μs and time window −3.5 to −1.8 μs similar to Figure 14. For Figure 17, the source was modeled to be at the center of tube 3, between tubes 12 and 13, tube 18, tube 23, and tube 28. For Figure 18, the source modeled at the center between tubes 2 and 3, tube 8, between tubes 12 and 13, tube 18, tube 23, and tube 28. The *e*-folding energy appears

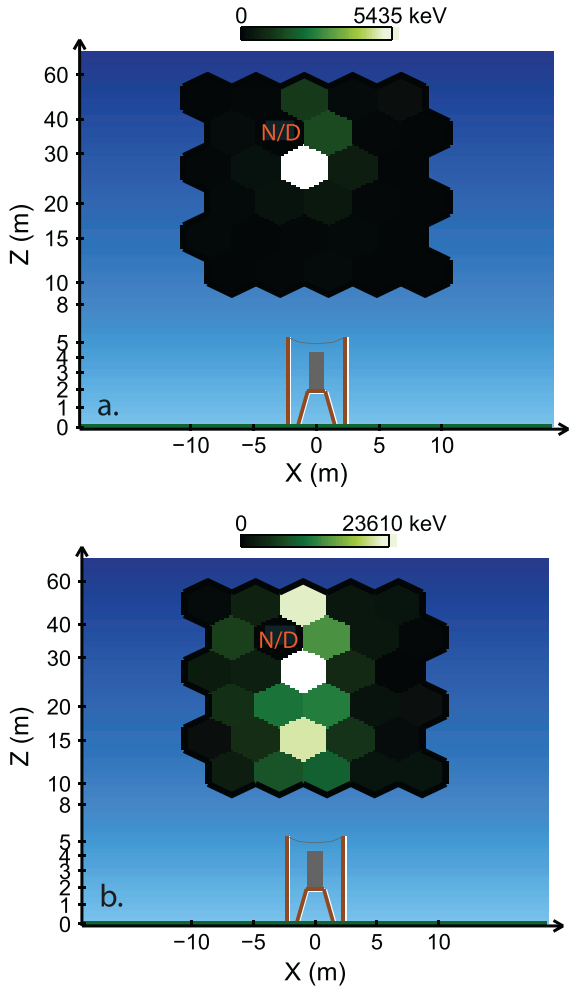

Figure 16. The X-ray emission of UF 11-35 L2 for two differing time windows. (a) The observation time exposures from −2.9 to −2.8 μs and (b) the observation time exposures from −3.5 to −1.8 μs including multiple altitude positions of the source. The X-ray source region moves downward through the entire FOV of the XCAM to make the pattern of illuminated tubes seen in Figure 16b.

to be close to 300 keV for these plots, and the general shape of the measured deposited energies appear to match the modeled deposited energies indicating a narrow source of emission. Figure 19 shows a 0.1 μs exposure time (−2.9 to −2.8 μs) of R_2/R_1 versus the radius of the source region using an analysis similar to Figure 12. Any *e*-folding energy below 150 keV the maximum source radius does not change significantly and so was not included in Figure 19. UF 11-35 L2 displays a maximum source region radius of 2.3 m. The results from Figure 19 also exclude *e*-folding energies higher than 700 keV.

4.2.4. Determining the Maximum Electric Charge of the Source Region

In order for a bright spot of X-rays to appear in only one of the XCAM's tubes (and no X-ray emission observed in any other tubes), runaway electrons must have propagated, lost energy, and stopped in a distance of no more than about 2 m (i.e., the radius of the source region corresponding to XCAM tube 18). In the case of UF 11-34 L1 and UF 11-35 L2, bright emission occurs in tube 18, while weak X-ray emission is observed in the surrounding tubes. It should be noted that a broken PMT sits adjacent to tube 18, so the X-ray emission could extend into that area. Runaway electrons, centered at the leader tip, are assumed to follow electric field lines that are spherically symmetric with an electric field $\mathbf{E} = -E(r)\hat{r}$ [*Bazelyan and Raizer*, 1998].

For $r < r_0$, the electrons will gain energy as long as $E > E_{th}$ where E_{th} is the RREA threshold field. Thus, to find the maximum radius that an electron will propagate, it is sufficient to start electron propagation at the surface ($r = r_0$) with $E = E_{th}$ assuming some initial kinetic energy, K_0 (note that the initial energy spectrum inside the sphere, $r < r_0$, is unknown, so the result remains unchanged when started at $r = r_0$). Outside that

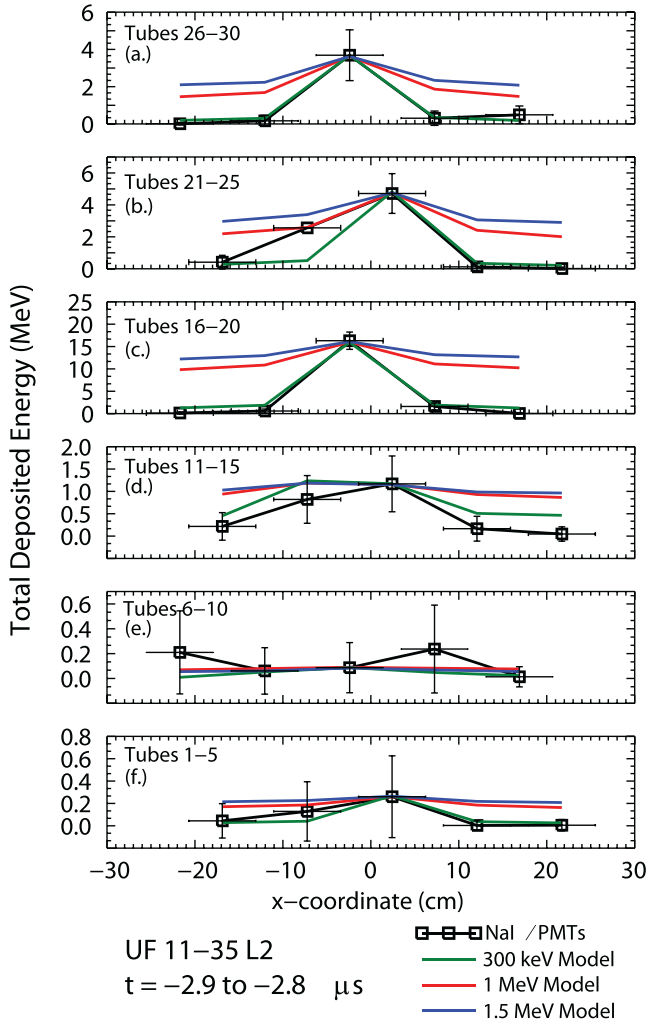

Figure 17. A −2.9 to −2.8 μs exposure (from UF 11-35 L2) of the lateral deposited energy distribution of the NaI/PMTs divided into six plots corresponding to differing altitudes. The models were chosen to have their sources centered at the following tubes: tube 28, tube 23, tube 18, between tubes 12 and 13, and tube 3.

sphere, $r > r_0$, the electric field falls off as $1/r^2$, i.e., all charge is assumed to be contained within the sphere. Even though $E < E_{th}$, electrons will still propagate some distance. The goal is to find r_0 and K_0 such that the electrons and hence X-ray emissions are consistent with the maximum source region radius found in the previous sections.

Specifically, $-E_{th}r_0^2/r^2$ is used for $r > r_0$. Figure 20 shows a projection of seven camera tubes (dashed circles) onto the source plane (in the *xz* plane). The source region and the radial electric field used in the model (arrows) are shown at the center of tube 18. As shown, the sphere contains a radius, r_0, with an electric field (arrows) outside falling off as $1/r^2$. Even though the size of the FOV in tube 18 differs in the *x* and *z* directions, spherical symmetry can be used because the source is assumed to be a sphere with most of its emission contained within the tube.

Since the source region is assumed to be a sphere with a radius, r_0, and the source charge is entirely contained in this sphere, then from Gauss's law an approximate total amount of the electric charge contained within that sphere can be estimated. Assuming a RREA threshold field and using the source region radius found from Figures 12 and 19, Gauss's law gives $q_{max} = 4\pi\epsilon_0 E_{th} r_0^2$. Using q_{max}, r_0, and the average downward leader speed, *v*, (found from Figure 9 for UF 11-34 L1 and estimated to be 10^7 m s^{-1} for UF 11-35 L2), the average charge density ($\rho = 3q_{max}/4\pi r_0^3$), the average charge per unit length ($\lambda = q_{max}/2r_0$), and the average current ($i = \lambda v$) can be estimated. For this calculation, we assume that r_0 remains the same size as the leader descends.

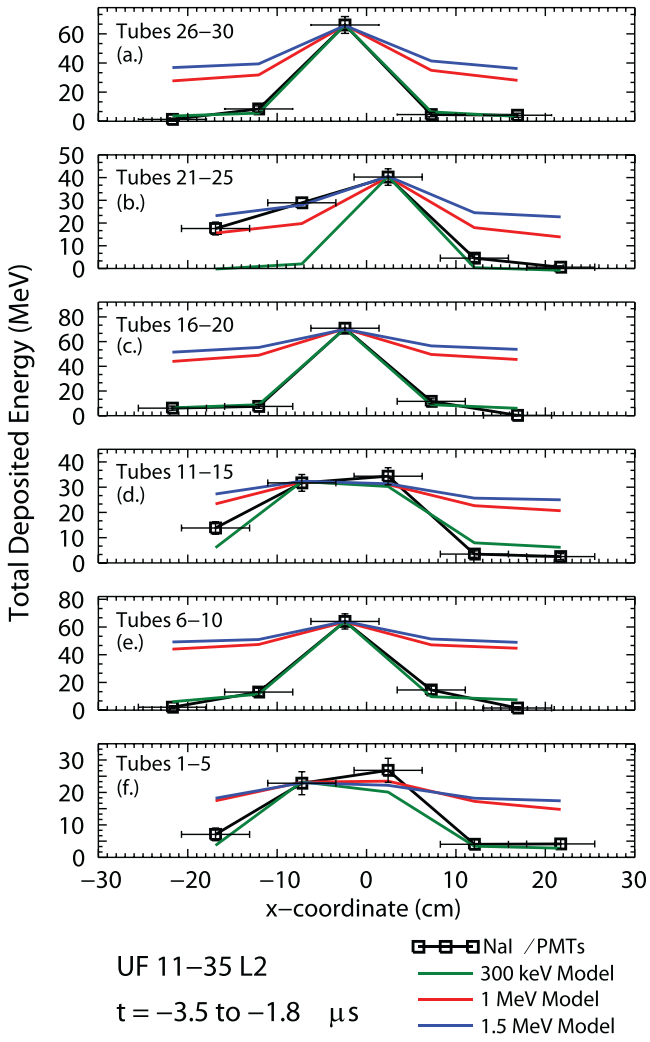

Figure 18. A −3.5 to −1.8 μs exposure (from UF 11-35 L2) of the lateral deposited energy distribution of the NaI/PMTs divided into six plots corresponding to differing altitudes similar to Figure 17. The models were chosen to have their sources centered at the following tubes: tube 28, tube 23, tube 18, between tubes 12 and 13, tube 8, and between tubes 2 and 3.

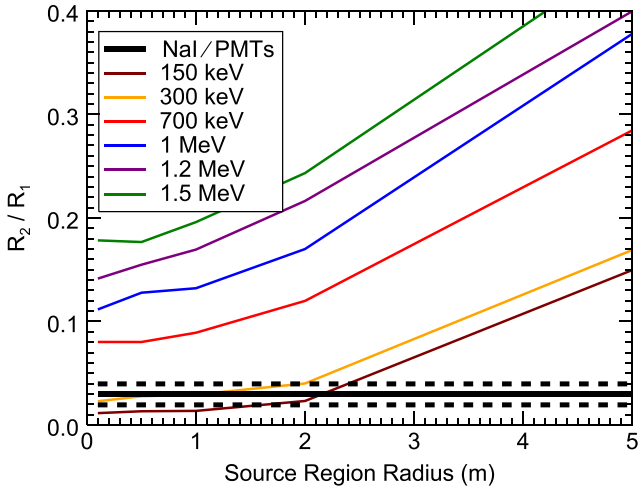

Figure 19. R_2/R_1 versus the source region radius similar to Figure 12 for the time window of −2.9 to −2.8 μs for UF 11-35 L2. The dashed lines indicate the error bars.

Using the above method, the maximum electric charge contained within the source region can be no greater than 2×10^{-4} C with a current on the order of 10^2 A for UF 11-34 L1. The charge density and charge per unit length are about 3×10^{-6} C m^{-3} and 4×10^{-5} C m^{-1}, respectively. For UF 11-35 L2, the maximum electric charge contained within the source region can be no greater than 2×10^{-4} C with a current on the order of 10^2 A. The charge density and charge per unit length are about 3×10^{-6} C m^{-3} and 4×10^{-5} C m^{-1}, respectively. It should be noted that the charges and average currents calculated are rough estimates, but the small differences between

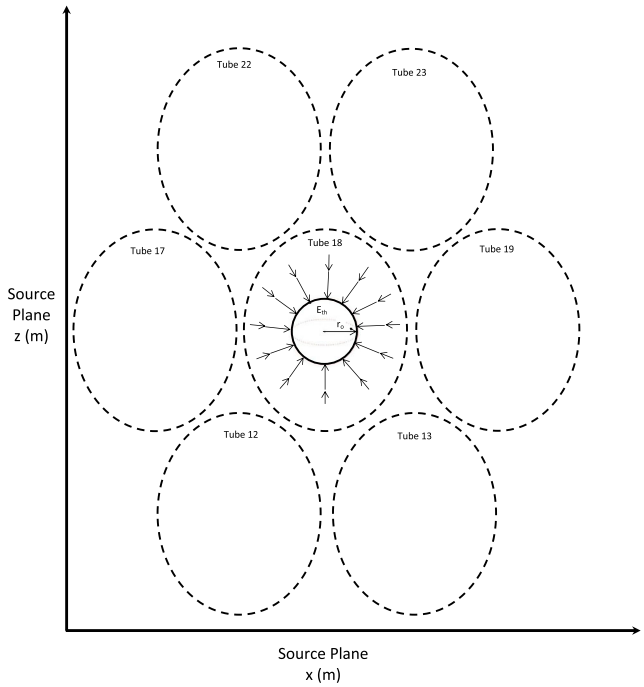

Figure 20. A projection of seven camera tubes (dashed circles) onto the source plane (in the *xz* plane). The source region and the radial electric field used in the model (arrows), $\mathbf{E}$=-$E_{th}\frac{r_0^2}{r^2}\hat{r}$, are shown at the center of tube 18. E_{th} is the RREA threshold field and r_0 is the radius of the sphere. The runaway electrons are emitted at r_0 and will travel in the direction opposite of the field lines, emitting X-rays, until they stop.

UF 11-34 L1 and UF 11-35 L2 could be because of the much higher peak currents in UF 11-35 L2 (18.4 kA) than in UF 11-34 L1 (13.4 kA).

5. Discussion Regarding the X-Ray Emission Patterns

Dwyer et al. [2011] observed a diffuse glow in the X-ray images from the XCAM from 2010 and suggested that the diffuse glow could be caused by (1) X-ray emission from a diffuse source, (2) hard X-rays penetrating through the surface of the lead shield, or (3) Compton scattering of X-rays emitted from the leader front. Based on the results presented here, the diffuse glow appears to be a combination of all three explanations.

First, UF 11-35 L5 appears to display X-ray emissions from a diffuse source or possibly emission from several sources. Several time frames from within UF 11-35 L5 show deposited energies that are not consistent with a point source of emission. Among those frames, a spraying distribution of X-rays can be seen (Figure 13g), which could indicate a nonuniform electron distribution around the lightning leader source. Another interesting example of a diffuse glow can be seen in Figure 13j. In the previous frame (Figure 13i), the X-ray source appears to be leaving the FOV. Figure 13j, just 0.1 μs later shows a bright glow in the XCAM's images of the lower eight tubes. This is likely due to the source region connecting to the tower during the attachment process. In Figure 13k, another 0.1 μs later, the diffuse glow appears to propagate upward at least 20–30 m, brightly illuminating nearly half of the XCAM's tubes. The appearance of an upward moving illumination has not been seen in any XCAM images before but could be explained by an upward spraying distribution of X-rays.

Interestingly, not all of the leaders investigated in this paper show a diffuse source of emission. Both dart-stepped leaders (UF 11-34 L1 and UF 11-34 L2 (not shown)) and one chaotic dart leader (UF 11-35 L2) show compact X-ray emission from their source regions. Since there are two distinct X-ray emission patterns (compact and diffuse) seen in this paper, this illustrates the variability of lightning leaders. It should be noted that the leaders (analyzed in this paper) that display diffuse X-ray emission patterns are associated with larger deposited energy fluxes. This implies that leaders with small deposited energy fluxes might also have a diffuse component, which is too weak to identify. In addition to establishing that some leaders exhibit compact X-ray source regions, their electron source region radii were also determined. The radius of

the source region was calculated for one time window of UF 11-34 L1 and UF 11-35 L2. For UF 11-34 L1 and UF 11-35 L2, the largest possible radii were determined to be 2.4 m and 2.3 m, respectively. Knowing the size of the source region can provide information about the runaway electron distribution, since X-rays are produced by energetic electrons. The runaway electron distribution can, in turn, help determine the lightning charge distribution. Furthermore, since the maximum source region radius was no greater than about 2.4 m for both leaders, we can infer that the radiation dose, from these two leaders, to be about 10^{-4} Sievert and hence the X-ray emissions from a direct strike would not be harmful [*Dwyer et al.*, 2010; *Schaal et al.*, 2012].

Second, hard X-rays penetrating through the front surface of the XCAM can be seen in the measurements from the 2010 leaders. By adding another lead shield to the front of the XCAM, the number of penetrating X-rays was reduced in the 2011 XCAM images, suggesting that the diffuse glow was partially caused by the transparent front of the XCAM.

Third, Compton scattering of X-rays, which was accounted for in all simulations, also was most likely involved. The effect of Compton scattering could not easily be seen in the data presented, but it is reasonable to infer that it could partially cause the diffuse glow.

6. Discussion Regarding the Maximum Charge of the Streamer Zone

The highest density of X-ray emissions is assumed to be associated with the X-ray source region and inferred to be emitted from the streamer zone in front of the leader. Following this assumption, the X-ray source region's maximum charge is likely the maximum charge contained within the streamer zone. Furthermore, the electric field for streamer propagation is about 500 kV/m [*Allen and Boutlendj*, 1991], which is greater than E_{th}. Thus, finding the source region radius r_0 also determines the maximum possible streamer zone charge and so calculations were made to quantify the maximum electric charge of the streamer zone. The maximum charge contained within this region for UF 11-34 L1 was determined to be no greater than about 10^{-4} C. For UF 11-35 L2, the maximum charge contained in the source region was no greater than about 10^{-4} C.

The magnitude of the maximum electric charge of all source regions investigated agrees with previous reports [*Krider et al.*, 1977; *Rakov and Uman*, 2003; *Celestin and Pasko*, 2011] that determined the charge could be no greater than 10^{-3} C. The maximum current was also calculated here to on the order of 10^2 A, which is slightly lower than other reports ($<$ 1 kA) [*Krider et al.*, 1977; *Rakov et al.*, 1998, *Rakov and Uman*, 2003; *Howard et al.*, 2010]. This paper also suggests that the leader channel core (composed of a large number of streamers) is responsible for the bulk transport of charge, which is in agreement with *Schonland* [1962] and *Bazelyan et al.* [2007].

Acknowledgments
We would like to thank those at Florida Tech and the University of Florida who assisted in the operation and maintenance of XCAM. This work was supported in part by NSF grant ATM 0607885, NASA grant NNX09AJ07H, and DARPA grants HR0011-08-1-0088 and HR0011-1-10-1-0061.

References

Allen, N. L., and M. Boutlendj (1991), Study of the electric fields required for streamer propagation in humid air, *IEE Proceedings-A*, *138*(1), 37–43.

Bazelyan, E. M., B. N. Gorin, and V. I. Levitov (1978), Physical and engineering foundations of lightning protection, *Leningrad, Gidrometeoizdat*, 223.

Bazelyan, E. M., Yu. P. Raizer, and N. L. Aleksandrov (2007), The effect of reduced air density on streamer-to-leader transition and on properties of long positive leader, *J. of Physics D: Applied Phys.*, *40*, 4133, doi:10.1088/0022-3727/40/14/007.

Bazelyan, E. M., and Yu. P. Raizer (1998), Spark discharge, *CRC Press*, Boca Raton. FL 215–234.

Biagi, C. J., D. M. Jordan, M. A. Uman, J. D. Hill, W. H. Beasley, and J. Howard (2009), High-speed observations of rocket-and-wire initiated lightning, *Geophys. Res. Lett.*, *36*, L15801, doi:10.1029/2009GL038525.

Biagi, C. J., M. A. Uman, J. D. Hill, D. M. Jordan, V. A. Rakov, and J. Dwyer (2010), Observations of stepping mechanisms in a rocket-and-wire triggered lightning flash, *J. Geophys. Res.*, *115*, D23215, doi:10.1029/2010JD014616.

Celestin, S., and V. P. Pasko (2011), Energy and fluxes of thermal runaway electrons produced by exponential growth of streamers during the stepping of lightning leaders and in transient luminous events, *J. Geophys. Res.*, *116*, A03315, doi:10.1029/2010JA016260.

Dwyer, J. R., et al. (2003), Energetic radiation produced during rocket-triggered lightning, *Science*, *299*, 694.

Dwyer, J. R. (2004), Implications of x-ray emission from lightning, *Geophys. Res. Lett.*, *31*, L12102, doi:10.1029/2004GL019795.

Dwyer, J. R., et al. (2005), X-ray bursts associated with leader steps in cloud-to-ground lightning, *Geophys. Res. Lett.*, *32*, L01803, doi:10.1029/2004GL021782.

Dwyer, J. R., and D. M. Smith (2005), A comparison between Monte Carlo simulations of runaway breakdown and terrestrial gamma-ray flash observations, *Geophys. Res. Lett.*, *32*, L22804, doi:10.1029/2005GL023848.

Dwyer, J. R. (2007), Relativistic breakdown in planetary atmospheres, *Phys. Plasmas*, *14*(042901), doi:10.1063/1.2709652.

Dwyer, J. R., D. M. Smith, M. A. Uman, Z. Saleh, B. Grefenstette, B. Hazelton, and H. K. Rassoul (2010), Estimation of the fluence of high-energy electron bursts produced by thunderclouds and the resulting radiation doses received in aircraft, *J. Geophys. Res.*, *115*, D09206, doi:10.1029/2009JD012039.

Dwyer, J. R., M. M. Schaal, H. K. Rassoul, M. A. Uman, D. M. Jordan, and J. D. Hill (2011), High-speed X-ray images of triggered lightning dart leaders, *J. Geophys. Res.*, *116*, D20208, doi:10.1029/2011JD015973.

Gorin, B. N., V. I. Levitov, and A. V. Shkilev (1976), Some principles of leader discharge of air gaps with a strong non-uniform field, *Gas Discharge, IEE Conf Publ.*, *143*, 274–8.

Howard, J., M. A. Uman, J. R. Dwyer, D. Hill, C. Biagi, Z. Saleh, J. Jerauld, and H. K. Rassoul (2008), Co-location of lightning leader x-ray and electric field change sources, *Geophys. Res. Lett.*, *35*, L13817, doi:10.1029/2008GL034134.

Howard, J., M. A. Uman, C. Biagi, D. Hill, J. Jerauld, V. A. Rakov, J. R. Dwyer, Z. H. Saleh, and H. K. Rassoul (2010), RF and X-ray source locations during the lightning attachment process, *J. Geophys. Res.*, *115*, D06204, doi:10.1029/2009JD012055.

Hill, J. D., M. A. Uman, and D. M. Jordan (2011), High-speed video observations of a lightning stepped leader, *J. Geophys. Res.*, *116*, D16117, doi:10.1029/2011JD015818.

Hill, J. D, M. A. Uman, D. M. Jordan, J. R. Dwyer, and H. K. Rassoul (2012), "Chaotic" dart leaders in triggered lightning: Electric fields, X-rays, and source locations, *J. Geophys. Res.*, *117*, D03118, doi:10.1029/2011JD16737.

Hill, J. D. (2012), The mechanisms of lightning leader propagation and ground attachment, Ph.D. Dissertation, University of Florida.

Idone, V. P. (1992), The luminous development of Florida triggered lightning, *Res. Lett. Atmos. Electr.*, *12*, 23–8.

Knoll, G. F. (2000), *Radiation Detection and Measurement*, John Wiley, Hoboken, New Jersey.

Krider, E. P., C. D. Weidman, and R. C. Noggle (1977), The electric field produced by lightning leader steps, *J. Geophys. Res.*, *82*, 951–60.

Lehtinen, N. G., T. F. Bell, and U. S. Inan (1999), Monte Carlo simulation of runaway MeV electron breakdown with application to red sprites and terrestrial gamma ray flashes, *J. Geophys. Res.*, *104*, 24,699–24,712, doi:10.1029/1999JA900335.

Petrov, N. I., and F. D'Alessandro (2002), Theoretical analysis of the processes involved in lightning attachment to earthed structures, *J. Physics D: Appl. Phys.*, *35*, 1788, doi:10.1088/0022-3727/35/14/321.

Rakov, V. A., et al. (1998), New insights into lightning processes gained from triggered-lightning experiments in Florida and Alabama, *J. Geophys. Res.*, *103*(D12), 14177–14130, doi:10.1029/97JD02149.

Rakov, V. A., and M. A. Uman (2003), *Lightning Physics and Effects*, Cambridge Univ. Press.

Saleh, Z., J. Dwyer, J. Howard, M. Uman, M. Bakhtiari, D. Concha, M. Stapleton, D. Hill, C. Biagi, and H. Rassoul (2009), Properties of the X-ray emission from rocket-triggered lightning as measured by the Thunderstorm Energetic Radiation Array (TERA), *J. Geophys. Res.*, *114*, D17210, doi:10.1029/2008JD011618.

Schaal, M. M., J. R. Dwyer, Z. H. Saleh, H. K. Rassoul, J. D. Hill, D. M. Jordan, and M. A. Uman (2012), Spatial and energy distributions of X-ray emissions from leaders in natural and rocket triggered lightning, *J. Geophys. Res.*, *117*, D15201, doi:10.1029/2012JD017897.

Schonland, B. F. J. (1962), Lightning and the long electric spark, *Adv. Sci.*, *19*, 306–313.